Scientific Report

Concerning the implementation of the project: January – November 2016

Within this period of time, the research work carried out within the frame of the project entitled *Interactional and functional effects of the substrate on the electrochemical behavior of micro and nanostructured metallic and oxidic deposits* was mainly directed towards two specific objectives: the development of new, active, platinum–carbon composites via liposomes-directed electrodeposition at conductive diamond and the use of conductive diamond powder as support for Pt-based electrocatalysts. The features making boron doped diamond highly suitable as electrode material were also investigated by computational experiments aiming to detect the local electron structure modifications induced in environment by a boron atom and the long range interaction between boron sites.

For this study, liposomes were prepared by the lipid film hydration method. The lipid mixture (phosphatidylcholine : cholesterol 10:1 w/w) was dissolved in chloroform, brought to a thin film in a rotary evaporator and then the film was hydrated with a solution of 65 mM chloroplatinic acid. Hand shaking, alternated with periods of brief sonication was applied before leaving the suspension to sit overnight and complete the swelling process. The obtained suspension was sonicated to reduce vesicle size, and materials not entrapped in vesicles were separated through dialysis. As-grown boron-doped polycrystalline diamond films were first subjected for 20 min to a mild anodic oxidation treatment (at 2.5 V in a 0.1 M $HClO_4$ solution) and then used as support for Pt electrochemical deposition, carried out at an applied potential of -0.3 V and by using 0.1 M $HClO_4$ as the supporting electrolyte. Two different deposition procedures were adopted. In the first case, in order to allow liposomes adsorption, BDD substrates were kept in contact for 24 hours with the as-prepared liposomal suspension then removed, immersed in the 0.1 M $HClO_4$ solution and subjected to cathodic polarization for 30 min. The second procedure consisted in the direct electrodeposition (at the same applied potential and polarization time) from 25 mL of 0.1 M $HClO_4$ solution in which 500 μL of liposomal suspension was added. Chronoamperometric curves were recorded during the deposition process and the integrated cathodic charge was used for the estimation of the platinum loadings. Electrodes obtained by the two methods will be further denoted as ADS and SOL, respectively. After electrodeposition, both types of electrodes were dried in air for two hours at 25 °C and

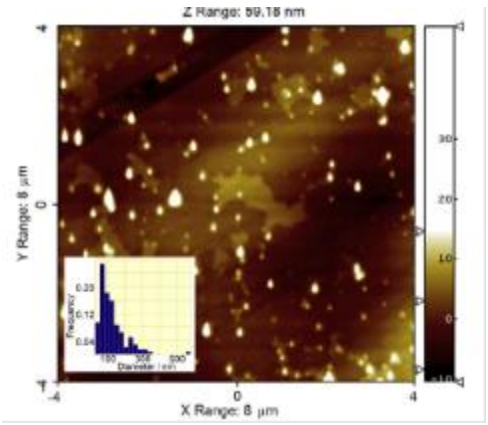

Fig. 1 AFM image of liposomes supported on freshly cleaved highly ordered pyrolytic graphite substrate. Inset: corresponding size distribution histogram.

heated up to 600 °C for five hours, in order to remove organic residues and to enable platinum exposure to electroactive species from the solution [26]. A slow heating rate of 1 °C min^{-1} was used to avoid sintering problems. Platinum electrodeposition was also carried out from a vesicle-free plating solution (0.1 M $HClO_4$ + 4.8 mM H_2PtCl_6), at the same applied potential, and the electrodes thus obtained were also used in some experiments, for comparison.

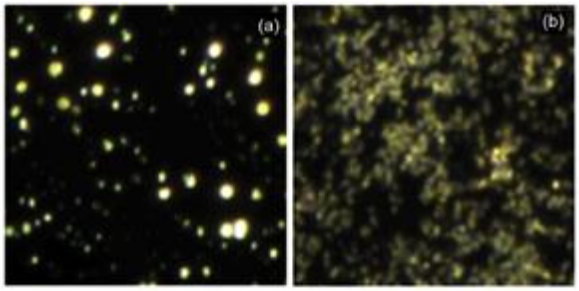

Fig. 2 Hyperspectral images of liposomes before (a) and after (b) platinum chemical reduction treatment. Scale: 3 cm = 50 μm.

After liposomes preparation, a small amount of the suspension was pipetted on freshly cleaved, atomically flat, highly ordered pyrolytic graphite (HOPG) substrates and examined by AFM. Fig. 1 shows a typical 2D AFM topographic image which clearly put into evidence the presence of quasi spherical vesicles, relatively uniform in size. Statistical analysis of the AFM images yielded for the size distribution Gaussian-like histograms (see the inset in Fig. 1) with a mean value of the liposomes diameter of 120 nm. In order to check the presence of the platinum precursor into the vesicles bulk, a fraction of the liposomal suspension was treated with an excess of 0.5 % $NaBH_4$ aqueous solution, and as a result, a large number of dark particles appeared, indicating chemical reduction of platinum ions to metallic species. Both before and after the reduction treatments, a few drops of the suspension were transferred on microscope slides, sealed with covers slips and then examined using an enhanced darkfield hyperspectral microscope system (CytoViva, USA). As hyperspectral images in Fig. 2 show, the reduction procedure led to the loss of the structural integrity of the liposomes and to formation of smaller nanoparticles with a more homogeneous size distribution. The main foreseen benefit of using liposomes as template for metal particles electrodeposition lies in the fact that it could allow, at least in principle, to control the size of the deposited particles by appropriately adjusting the size of precursor-containing vesicles. In our case, by taking into account an average diameter of 120 nm (as estimated by AFM) and by assuming a steric bilayer thickness of *ca*. 42 Å, an inner volume of the liposomes of *ca*. 7.3×10^5 nm^3 can be calculated. Moreover, based on its octahedral structure, the estimated volume of a $[PtCl_6]^{2-}$ ion is of *ca*. 1.16 nm^3, since radii of Cl^- and Pt^{4+} ions are 1.8 Å and 0.625 Å, respectively, and the typical length of the Pt–Cl bond is 2.3 Å. Keeping in mind that, for random packing, the fraction of the liposome volume occupied by chloroplatinic ions is 0.64, and by assuming a spherical shape of the deposited particles, an average size of the latter of *ca*. 22.5 nm can be roughly estimated.

After the electrodeposition and subsequent thermal treatments (see Material and methods Section) the Pt-modified BDD electrodes were examined by SEM and Fig. 3 shows characteristic micrographs obtained both for ADS and SOL (Figs. 3a and 3b, respectively)

together with a typical image of an electrode obtained by using a vesicle-free plating solution (Fig. 3c). It appeared that, when using liposomes as templates, electrochemical deposition results in the formation of much smaller platinum particles which might be beneficial in terms of the efficiency of noble metal utilization since it ensures a larger number of active sites in a small volume. It was also found that, for both ADS and SOL electrodes, the size of deposited particles ranges between *ca*. 15 and *ca*. 40 nm, in rather good agreement with the theoretically estimated average size (see above). This feature is important because it demonstrates the existence of a direct relationship between the volume of precursor-containing liposomes and the size of the electrodeposited metal particles. As Fig. 3b indicates, when the electrodeposition was carried out without prior adsorption of the liposomes, the majority of the Pt particles are partially embedded in some carbonaceous irregular structures, most likely formed by thermal degradation of the vesicles walls. Surprisingly, the surface of ADS electrodes is free of such problems and a more uniform Pt distribution was observed in this case, although the presence of some spherical composite aggregates was also evident (Fig. 3a).

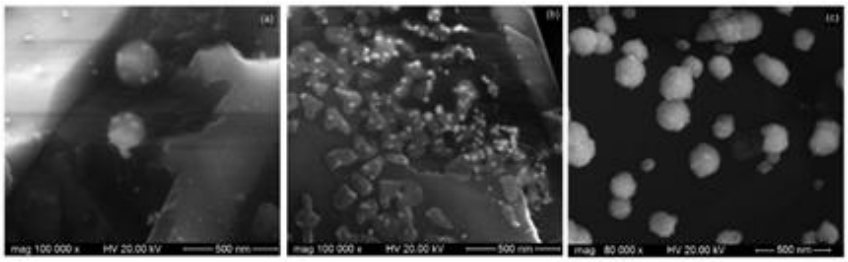

Fig. 3 Characteristic SEM micrographs for ADS (a) and SOL (b) electrodes and for electrodes obtained by platinum electrodeposition from a vesicle-free plating solution (c). Platinum loading (μg cm^{-2}): (a) 24.3; (b) 43.2; (c) 58.4.

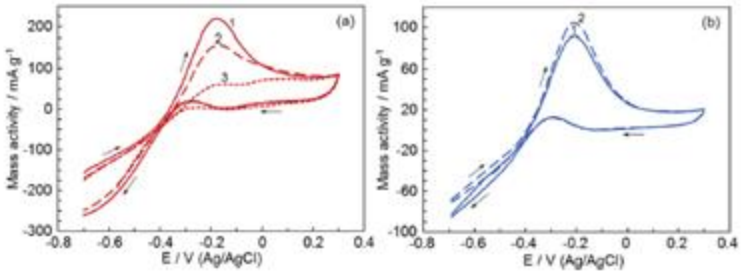

Fig. 4 Cyclic voltammograms recorded in a 1M NaOH + 4.1 M CH_3OH solution (sweep rate, 35 mV s^{-1}) at ADS electrodes (a) during the 1st (1), 2nd (2) and 3rd (3) cycles and at SOL electrodes (b) during the 1st (1) and 30th (2) consecutive runs.

In order to appraise the electrocatalytic activity of platinum-decorated electrodes obtained by liposome-assisted electrodeposition, methanol anodic oxidation in alkaline media was used as a test reaction and Fig. 4 shows typical cyclic voltammograms recorded in a 1 M NaOH + 4.1 M CH_3OH solution (sweep rate, 35 mV s^{-1}) both at ADS and SOL electrodes (Figs. 4a and 4b, respectively). Due to the particular obtaining conditions, the electrocatalyst loading as well as the morphology of the deposits are not the same for the two types of electrodes and this is why, to better put the results into perspective, the voltammetric current was expressed in terms of mass activity (measured current divided by the deposited Pt mass). It was observed that the peak current recorded for methanol oxidation during the first anodic scan is *ca*. 2.4 times higher at the ADS electrodes than at the SOL ones (compare curves 1 in Fig. 4), probably due to the fact that, at the time scale of the voltammetric experiments, platinum particles partially embedded in the carbonaceous matrix are less accessible to electroactive

species from the solution. Conversely, SOL electrodes are free of such problems (see Fig. 4b) which indicates that during methanol oxidation in alkaline media platinum is less sensitive to deactivation (*e.g.*, via CO poisoning) when deposited from the liposome suspension without prior adsorption. Furthermore, the slight increase of the peak current after 30 consecutive voltammetric runs observed at SOL electrodes suggests that continuous cycling results in this case in a non-negligible enhancement of the electrochemically active surface area of the electrocatalyst, probably due to the fact that wetting is somewhat promoted during potential cycling.

The particularly compact structure of polycrystalline diamond layers inherently leads to a rather low specific surface area of deposited electrocatalysts which limits to a certain extent possible practical applications of such systems. However, the possibility exists, at least in principle, to eliminate this drawback by using as substrate conductive BDD powder instead of a continuous conductive diamond film. As stated in the previous report, the boron-doping level of the (111) crystallites from the polycrystalline diamond is *ca*. 10 times higher than that of the (100) ones which inherently leads to an inhomogeneity of the surface in terms of conductivity and, consequently, to a nonuniform electrodeposition of platinum particles. The use of relatively large area films enables neglecting such effects because, usually, the two different types of crystallites are evenly distributed over the surface and the observed overall activity is in fact an average one. Conversely, when micrometric particles are used it is highly desirable that this inhomogeneity is somewhat mitigated in order to have a distribution of the deposited particles as uniform as possible. To this aim, within the frame of the present project two different approaches have been used: the embedment of the BDD powder (BDDP) into a SiO_2 veils (SiO_2V) matrix and its surface modification by iridium oxide thermal deposition.

For obtaining the boron-doped diamond powder–SiO_2 veils composite (BDDP–SiO_2V), a suspension containing *ca*. 5 mg of BDDP, 5 mL ethanol and 1 mL ultrapure water was ultrasonicated for 30 min and added to an aqueous ammonium tartrate-tetraorthosilicate (Alfa Aesar, 99%) mixture. The obtained slurry was allowed to stay for 3 h for ageing, then filtered, dried and thermally annealed in air at 500 °C. To prepare working electrodes, a 1.8 mg sample of nanoparticles to be investigated (BDDP or BDDP–SiO_2V) was mixed with Nafion (9 μL, 5 vol%) and isopropyl alcohol (450 μL), the suspension obtained being sonicated for 3 h. Twenty microliters of suspension was pipetted out and delivered onto a glassy carbon surface, the coated electrodes were dried in air at room temperature and then were further used as substrates for platinum deposition. The deposition was carried out electrochemically, from a 0.5 M H_2SO_4 + 4.5 mM H_2PtCl_6 solution, by applying several consecutive potentiostatic pulses of five seconds' duration each (applied potential, –0.15 V). For both types of Pt-modified electrodes thus obtained (Pt/BDDP and Pt/BDDP–SiO_2V) the noble metal loading was then calculated from the cathodic charge integrated during electrodeposition.

Fig. 5 shows SEM images of the boron-doped diamond powder and of the composite obtained by its embedment into the silica structure (Figs. 5a and 5b, respectively). It appears that diamond particles are rather uniform in size (*ca*. 300 to 500 nm), although a small number of larger particles (or particle aggregates) can be also observed. The BDD−SiO_2V composite consists in a veillike silica matrix surrounding the BDD particles, which, as Fig. 5b illustrates, tend to agglomerate partially. Keeping in mind that, due to the presence of hydroxyl and Si−O^- groups, SiO_2 surfaces are typically negatively charged, it seems likely to assume that this inhomogeneity is the result of some electrostatic repulsion between the silica structure and the oxidized BDD nanoparticles. The nature of the carbon species was investigated by XPS and it was found that in both cases the deconvoluted C 1s core level spectra display, besides the peak characteristic to bulk diamond (BE, 283.5 eV), four additional ones at higher *BE* values (see upper insets in Fig. 5). The second peak (*BE*, 284.8 eV), originating from carbon atoms close to the surface, can be ascribed to nondiamond carbon. At binding energy values of 285.5 eV, 288.2 eV and 289.7 eV three other subpeaks were also observed after deconvolution and were ascribed to the presence of carbon bonded to oxygen, *i.e*., C–OH and C–O–C, C═O, and O═C–O, respectively. As expected, for the BDDP sample sp^3 diamond carbon prevails (relative surface concentration 68.9%), whereas in the case of the BDDP−SiO_2V composite the major contribution (67.2%) to the C 1s spectrum is given by the peak at 284.8 eV, because precursors employed for the synthesis of the silica matrix are obviously additional sources of nondiamond carbon species. It is also worthy of note that the overall surface concentration of oxygenated carbon species is *ca*. 1.8 times higher for BDDP−SiO_2V than for the conductive diamond powder (*ca*. 23.3% compared to *ca*. 12.9%). These findings could be meaningful because the

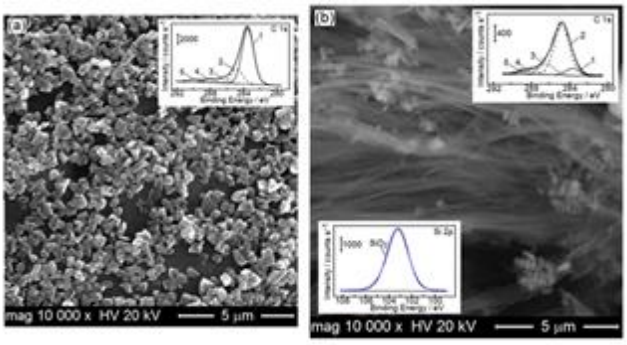

Fig. 5 SEM images of BDDP (a) and of the composite obtained by its embedment into the silica structure (b). Upper insets: corresponding XPS spectra in the C 1s region: (1) diamond; (2) nondiamond surface carbon; (3) carbon singly bonded to oxygen; (4) C═O; (5) O═C–O. Lower inset: narrow-scan XPS spectrum recorded for the composite in the Si 2p region.

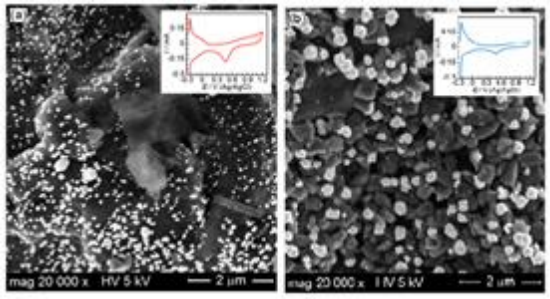

Fig. 6 SEM micrographs for Pt/BDDP−SiO_2V (a) and Pt/BDDP (b) electrodes. Insets: stable cyclic voltammograms recorded in 0.5 M H_2SO_4 at a sweep rate of 20 mV s^{-1}. Pt loading (μg cm^{-2}): (a) 11.2; (b) 10.8

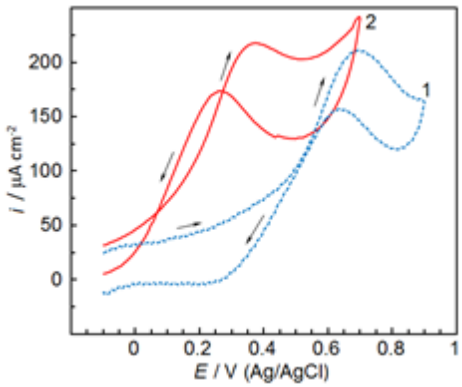

Fig. 7 Cyclic voltammograms recorded in a 0.5 M H_2SO_4 + 2.5 M CH_3OH solution (sweep rate 20 mV s^{-1}) for Pt/BDDP (1) and Pt/BDDP−SiO_2V (2).

presence of oxygen-containing groups on carbonaceous substrates affects the electrocatalytic deposits both in terms of morphology and activity. Narrow-scan XPS spectrum recorded for the composite in the Si 2p region (bottom inset in Fig. 5b) exhibited a rather symmetrical peak located at *ca*. 103.3 eV which is clear indication of SiO_2 presence. After platinum deposition, both Pt/BDDP−SiO_2V and Pt/BDDP electrodes were subjected to several consecutive cyclic voltammetric experiments in 0.5 M H_2SO_4 (potential range, −0.25 to 1.2 V, sweep rate, 20 mV s^{-1}) until a stable response was recorded. Fig. 6 shows characteristic micrographs obtained, after stabilization, for the above electrodes with similar platinum loadings. It was observed that, unlike BDDP, the use of a BDDP−SiO_2V substrate allows the deposition of much smaller and better dispersed Pt particles (ranging from *ca*. 45 nm to *ca*. 140 nm) although the presence of a small number of larger clusters (*ca*. 345 nm) is also evident (Fig. 6a). As insets from Fig. 6 show, both types of electrodes exhibit after stabilization voltammetric responses similar in shape, typical of platinum behavior in acidic media, which allowed the estimation of the active surface area of the Pt deposits. Values thus obtained were hereinafter used to normalize recorded voltammetric currents. As a means to gauge the influence of the BDDP−SiO_2V support, methanol anodic oxidation was selected as test-reaction and the activity of the electrodes was checked by cyclic voltammetry. Typical responses recorded for electrodes with similar platinum loadings (*ca*. 12 μg cm^{-2}) during the fifth consecutive voltammetric run in a 0.5 M H_2SO_4 + 2.5 M CH_3OH solution (sweep rate, 20 mV s^{-1}) are shown in Fig. 7. It was found that for Pt/BDDP electrodes (curve 1) the main forward anodic peak (corresponding to methanol oxidation on the oxidized platinum surface) is located at *ca*. 0.7 V, in very good agreement with the results reported for Pt electrochemically deposited on BDD nanoparticles obtained by mechanical crushing of BDD films. As curve 2 from Fig. 7 emphasizes, at Pt/BDDP−SiO_2V electrodes a significant negative shift (*ca*. 0.35 V) of this peak appeared, which is incontrovertible proof that the presence of the silica matrix induces considerable improvement in the overall methanol oxidation kinetics. To assess the effect of the presence of SiO_2 on the resistance to

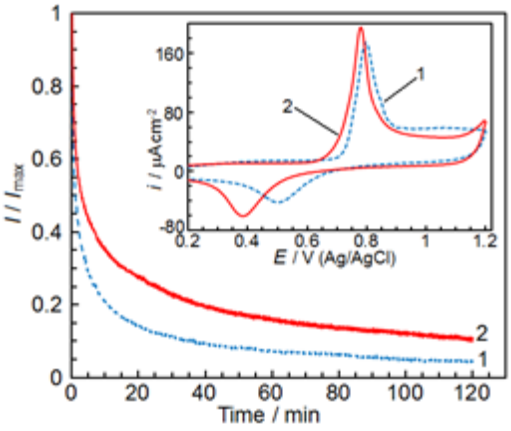

Fig. 8 Chronoamperograms for methanol oxidation recorded in 0.5 M H_2SO_4 + 5 M CH_3OH at Pt/BDDP (1) and Pt/BDDP−SiO_2V (2). Applied potential (V): 0.5 (1) 0.2 (2). Inset: corresponding stripping voltammograms of adsorbed CO recorded in 0.5 M H_2SO_4 at a sweep rate of 20 mV s^{-1}.

fouling during methanol oxidation of the platinum particles, long-term polarization measurements were also carried out in a 0.5 M H_2SO_4 + 5 M CH_3OH solution. For better comparison of the results, the applied potential was that corresponding to the half-peak value and the oxidation current (I) was normalized by its maximum value (I_{max}). Typical chronoamperometric responses recorded for the two types of electrodes (Fig. 8) have shown that after two hours of continuous electrolysis the oxidation current at Pt/BDDP reached *ca*. 5% of its initial value, whereas that for the platinum supported on BDDP−SiO_2V decreased only to *ca*. 11%. This behavior indicates that the use of the composite substrate also improves to some extent the resistance to deactivation (probably by CO poisoning) of the platinum particles. Electrochemical oxidation of adsorbed carbon monoxide was also investigated and the inset in Fig. 8 shows typical anodic stripping voltammograms recorded for both Pt/BDDP and Pt/BDDP−SiO_2V electrodes (curves 1 and 2, respectively). In the latter case, a relatively significant cathodic shift of the onset potential of CO oxidation was observed (*ca*. 100 mV), demonstrating that, for composite-supported platinum particles, CO desorption is somewhat facilitated.

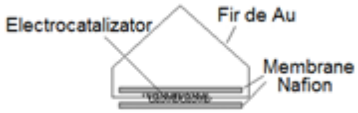

Fig. 9 Schematic diagram of the porous gas-diffusion-type electrodes based on BDDP.

Another approach to enhance the efficiency of the BDDP-supported electrocatalysts consisted in the modification of the powder substrate by a thin layer of iridium oxide, prior to electrochemical deposition of the platinum. For this end, *ca*. 200 mg BDDP were mixed under stirring with 590 μL 0.5 M H_2IrCl_6 and 500 μL isopropyl alcohol and, after the evaporation of the solvent, the mixture was thermally treated for 2 h at 300 °C. After cooling, the resulting agglomerates were ground in an agate mortar and then added into a preheated solution obtained from 500 μL ethanol and 500 μL 65 mM H_2PtCl_6. The solvent was again evaporated and *ca*. 14 mg of the resulting solid residue was mixed with 82 μL Nafion 5% and 24 μL de Teflon suspension 6%. The paste was then spread and pressed between two small wet sheets of Nafion membrane. A thin gold wire was also pressed into the paste for electrical contact (Fig. 9). This type of assembly (Fig. 10a) was used in the "*floating electrode*" configuration, i.e., it was suspended on the surface of the electrolyte solution (Fig. 10b). The deposition of the platinum was performed by continuously cycling the potential of the floating electrodes (scan rate 20 mV s-1) within the potential range 0.6 ÷ -0.25 V in in a nitrogen-saturated 0.5 M H_2SO_4 solution. Cyclic voltammograms were recorded, and the deposition process was continued until a stable voltammetric response was obtained (typically after *ca*. 40 cycles).

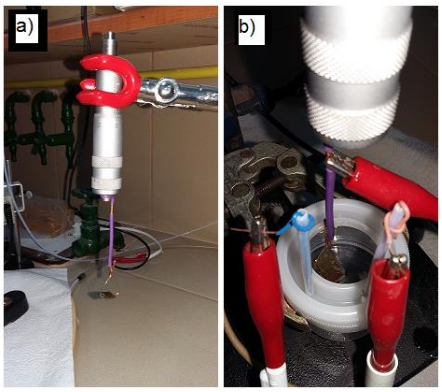

Fig. 10 Pt/IrO_2/BDDP floating electrode (a) and the experimental setup for electrochemical experiments (b).

After platinum deposition, the electrodes were suspended for one hour in distilled water in order to remove remaining traces of the Pt salt.

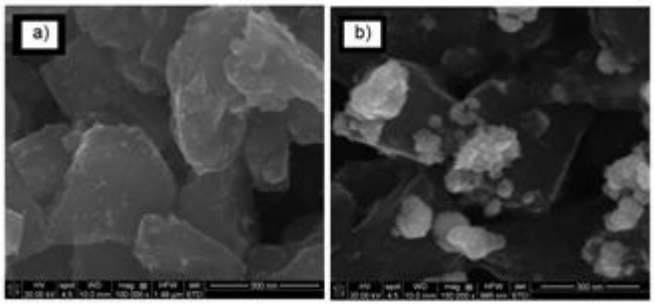

Fig. 11 SEM images for IrO_2/BDDP (a) and Pt/IrO_2/BDDP (b).

Fig. 11 shows SEM images obtained for IrO_2/BDDP before (a) and after platinum electrodeposition (b). It was observed that this process resulted in the formation on the IrO_2-modified BDD grains of small, rather uniform in size (30 to 75 nm) platinum particles, although the presence of larger clusters (up to *ca*. 150 nm) is also evident. In order to evaluate the electrochemically active surface area of the platinum deposit the electrodes were suspended on a 1 M NaOH solution and cyclic voltammograms were recorded until a stable response was obtained (curve 1 from Fig. 12). Although the voltammograms seem to be affected to some extent by the presence in the bulk of the electrodes of Teflon particles (that may lead to a less good electrical contact between diamond micrometric grains), their shape allow the estimation of the active area, the values thus obtained being further used to normalize the current.

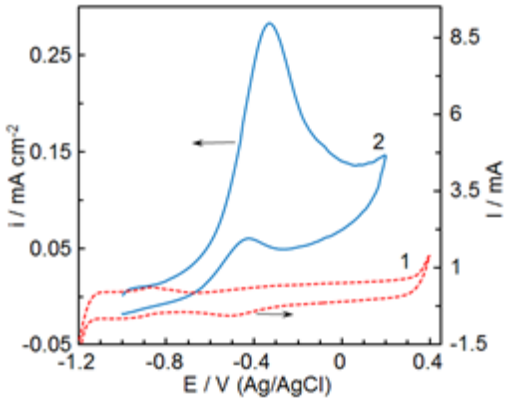

Fig. 12 Cyclic voltammograms (20 mV s^{-1}) at Pt/IrO_2/BDDP porous gas-diffusion-type electrodes recorded in NaOH 1M in the absence of methanol (1) and at a concentration of 1.23 M.

To assess the electrocatalytic activity of the three dimensional electrodes methanol oxidation was selected again as test reaction and the electrodes were suspended on the surface of a 1 M NaOH solution containing a concentration of 1.23 M CH_3OH. We should emphasize that such configuration provides a means of testing the electrochemical behavior in an environment that approximates that in an actual fuel cell, although in the present case the ambient temperature was used, rather than the 80–100 °C range typical for an operating polymer electrolyte fuel cell. Results thus obtained are illustrated by curve 2 from Fig. 12 which shows the voltammetric response recorded for methanol oxidation during the fifth consecutive scan. It was observed that, although the methanol concentration is only 1.23 M, the value of the peak current is similar to that recorded at Pt/BDDP for a two times higher concentration (Fig. 7) which demonstrates the advantages of using porous gas-diffusion-type electrodes. Cyclic voltammetry experiments also shown that at Pt/IrO_2/BDDP electrodes the main anodic peak for methanol oxidation (at *ca*. -0.3 V) is with more than 100 mV lower than that recorded for the same process taking place at Pt/Co_3O_4/BDD electrodes or at the Pt-carbon composites obtained from liposomal systems. This behavior clearly indicates that

the presence of the iridium oxide intermediary layer leads to the improvement of the kinetics of methanol oxidation overall process at the surface of the Pt particles.

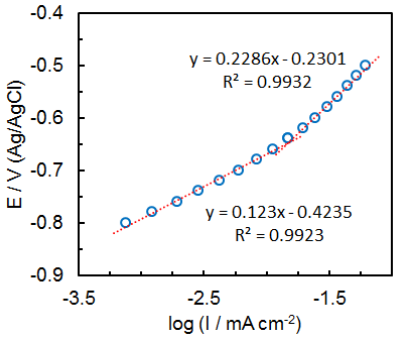

Fig. 13 Results of the steady-state measurements obtained in NaOH 1M + CH_3OH 1.23 M solution at Pt/IrO_2/BDDP electrodes.

In order to appreciate the possible practical utility of such electrodes, steady-state polarization measurements were also performed (in the same 1 M NaOH + 1.23 M CH_3OH solution, under stirring conditions) by applying increasingly positive potentials in 20 mV steps and then waiting for 5 min for the current to stabilize. As higher potential values are only of a limited interest for applications, Fig. 13 shows a Tafel plot typical of the behavior observed for the floating electrodes electrodes below -0.4 V *vs*. Ag/AgCl. Obviously, without further detailed work the Tafel slopes measured under these conditions (*ca*. 120 mV decade^{-1} below -0.65 V and *ca*. 230 mV decade^{-1} at higher potentials) cannot be used directly to infer mechanistic details. We should note, however, that values around 118 mV decade^{-1} indicate the break of the first C–H bond from the methanol molecule as rate-determining step. At higher potentials, the doubling of the Tafel slope suggests a slower transfer of the reactant and/or of the reaction product towards/from the electrocatalyst surface and consequently a less efficient utilization of the available active sites.

At the present stage of our research, we are also proposing several numeric experiments aiming to detect particularities induced by the boron atom in an environment resembling diamond lattice, in order to understand the functionality of boron doped diamond electrodes. Whether the first expectation would be to tackle this problem with band structure methods, we will opt for a molecular insight, choosing instead a solid body large carbon molecule with one or two nodes occupied boron atoms. This strategy benefits from enhanced leverages in the design of computation set-up and more illuminating analysis tools. The calculations were done by Density Functional Theory (DFT), using Gaussian code, with the 6-31G basis set and the B3LYP and the BP86 functionals.

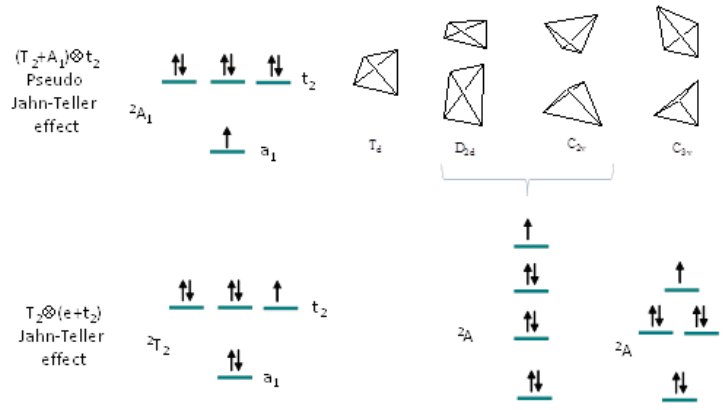

Fig. 14 Qualitative synopsis of the first and second order Jahn-Teller effects determined by the degenerate groundstate from incomplete shells of electron deficient boron site in tetrahedral environment.

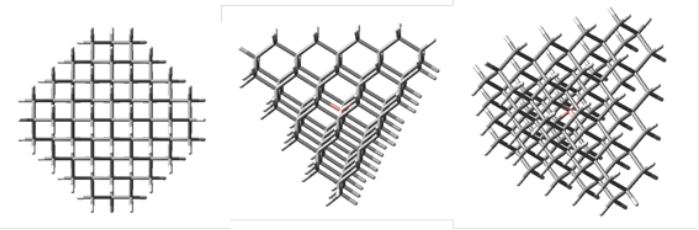

Fig. 15 Different orientation of the $BC_{86}H_{76}$ molecule with T_d symmetry, having a central boron atom.

Starting from qualitative reasons, one may assume the existence of a Jahn-Teller effect on the electronic system around the boron atom, as sketched in the synopsis from Fig. 14. Namely, extrapolating the electronic structure of the methane as roughly representing the situation of the carbon atom in large tetrahedral clusters or in the bulk of the diamond, one may expect a triple degenerate set as highest occupied molecular orbital (HOMO) with t_2 label in the T_d point group. Replacing the central carbon atom with a boron, a hole is produced in the HOMO level, forming then a $^2T_2$ degenerate ground term. The Jahn-Teller effect is the spontaneous breaking of the high symmetry when the system formally meets degenerate groundstate, a geometry distortion leading the system to lower symmetry and a non-degenerate finality. The consecrated labelling of the effect occurring on a triple degenerate state in tetrahedral point group is $T_2\times(e + t_2)$, the first label standing for the electronic groundstate, while the parenthesis describes the distortion coordinates. In very approximate manner, skipping the mathematical details, the distortions can be described as compression or elongation of the tetrahedron from different directions, leading for instance to D_{2d} symmetries if this occurs along a second order axis, or to C_{3v} pyramids in the case of third order axes. Besides, there is the possibility of a second order interaction (pseudo Jahn-Teller effect), implying the interaction between groundstate and an excited level, via molecular distortions. Here, the excited state can be formulated as the movement of the hole deeper in the closed shell, taking heuristically the a_1 function which describes altogether with the t_2 set the representation of four hybrid orbitals from tetrahedron. In general, the pseudo Jahn-Teller effect implies non degenerate groundstate, but this we have the reverse situation. The implication of higher order of interaction is demanded because the nominal Jahn-Teller effect gives rise to only to non-polar distortions, while the computed mapping showed polar coordinates too. For instance, in the synopsis from Fig. 14, the non-polar coordinates are figured by the D_{2d} distortions of the tetrahedron with equal angles in opposed halves, while a polar route enables the C_{2v} tetrahedron with different RBR and R'BR' angles for the $R_2BR'_2$ central site.

For the quantitative verification of the possible Jahn-Teller effect we draw the potential energy surfaces and curves taking the $BC_{86}H_{76}$ and $BC_{50}H_{52}$ molecules, with tetrahedron shape and spanning the T_d point group. In the given composition, the test molecules would mimic boron doped at concentrations of about 1% and 2% in the diamond crystals. A first check will consist in taking the boron atom from $BC_{86}H_{76}$ in off-center position, in orientations scanning a mesh of polar angles, θ and φ. The calculation was done by the B3LYP functional and the 6-31G basis set. After drawing the maps at three amplitudes of this shift, namely *dr*=0.05 Å, 0.10 Å and 0.15 Å, the minimum with respect the radial

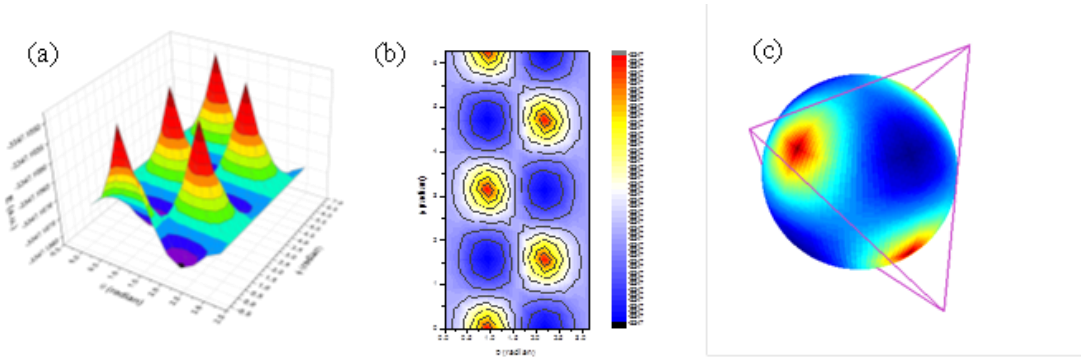

Fig. 16 Different representations for the potential energy surface mapping the orientations of the off-center displacement of the boron atom in the $BC_{86}H_{76}$ molecule. a) potential energy surface with θ and φ polar angles in abscissas. b) The contour of energy surface in the θ and φ coordinates. c) The color map representation of the energy on the sphere (with θ as coordinates for parallels and φ running on the meridians); the tetrahedron shows the environment towards which the boron atom takes the acentric displacements.

coordinate was interpolated, at each point of the considered θ and φ coordinates. The minima of *dr* dependences are varying between the 0.04 Å and 0.11 Å, suggesting relatively small distortions. The sharp peaks from the panel (a) of the Fig. 16 suggest the Jahn-Teller effect, these points falling in the proximity of the degenerate states. The panel (c) shows the color map on the coordination sphere of the boron atom, having also the reference of tetrahedral placement of the neighbor atoms (i.e. the carbon sites of the BC_4 moiety). One may see that the maxima, marked in red coloring are occurring when the off-center displacement goes in the direction tetrahedral vertices. Conversely, the energy minima are found in the opposed direction, when the central atom and a tetrahedron face trend toward a slightly more flattened BC_3 prism. This situation can be intuitively understood as a solution to the electron deficiency of the boron center. Having only three valence electrons, the boron cannot equivalent establish bonds with all the four carbon neighbors, preferring a tighter relationship with a set of three, approached in the course of such an off-centric displacement. The points placed at two-fold symmetry axes with respect the tetrahedron are saddle points, the potential energy surfaces having positive curvature on the axis between vertices and negative on the road connecting the minima between the neighbour faces. An interesting fact is that the described energy landscape is rather shallow, with a gap of about 3 kcal/mol between minima and maxima. This is somewhat surprising for a balance implying the redistribution of covalent bonds. It can be taken as an indicative that the frustration due to the electron deficiency of the boron is not kept local, being shared tough delocalization by larger portions of the lattice. This comes in the support of the idea that the hole formally originating from the boron can act as contributor to electronic conduction.

The previous mapping was confined to frozen geometry of the assembly, imposed from the optimization of the $C_{87}H_{76}$ molecule. To refine the account of geometry factors, we considered a relaxed potential energy surfaces, containing only one or two bond angles of the central BC_4 tetrahedron, while the whole molecule is allowed to converge at new geometry, at each point of the scanned variation. Because this procedure is somewhat time

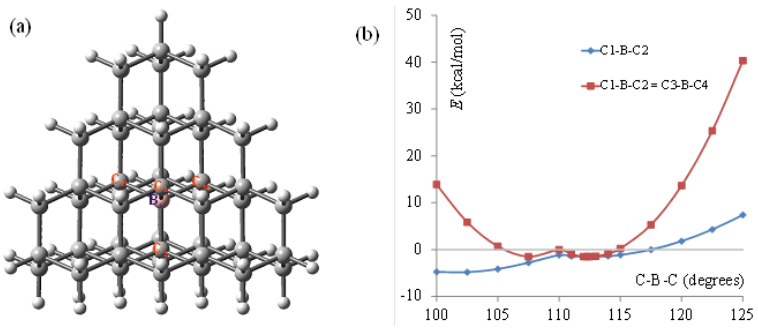

Fig. 17 The $BC_{50}H_{52}$ molecular model (panel a) and the results of relaxed potential energy curves tuning selected angles in the central BC_4 tetrahedron (panel b).

consuming, we confined ourselves to a smaller probe molecule, $BC_{50}H_{52}$ (see Fig. 17). The relaxed potential energy-surface was taken first running a D_{2d} distortion, imposing equal two angles from the BC_4 tetrahedron, placed in opposed halves and mutually orthogonal planes. The resulted symmetrical curve with local maximum nearby the regular tetrahedron angle (~109.5°) resembles the sections in the Jahn-Teller potential energy surfaces (see Fig. 17). The minima, occurring at deviations with about ±2.5 degrees, are very shallow, with small stabilization of ~1.5 kcal/mol with respect of the central peak. The small energy intervening in the effect is in line with the conclusion from the above discussion. To be distinguished from the previous full potential surface scan, the imposed distortion is non-polar. Allowing a polar deformation of the tetrahedron, only one C-B-C angle is fixed, while the other one, as well as all the other geometry variables are optimized. The resulted curve is placed below the previously drawn one, suggesting a further stabilization coming from the combination of first and second order Jahn-Teller effects. A minimum with about -5 kcal/mol relative stabilization is visible at the 102.5° angle. This can be heuristically interpreted as a certain preference to form B-C bonds having slightly higher p content in the hybrids than the regular s:p=1:4 ration in the sp^3 tetrahedron scheme.

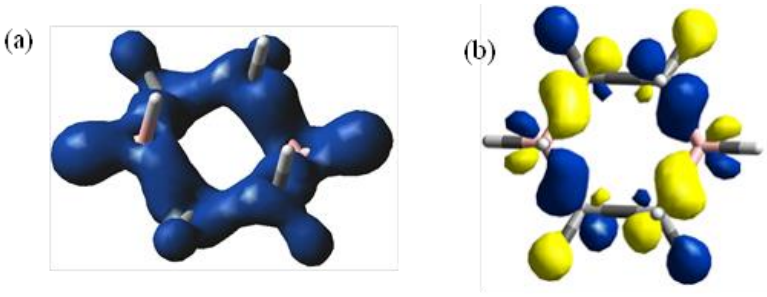

Fig. 18 The spin density maps for the $C_4H_8B_2H_4$ determined from unrestricted B3LYP/6-31G calculations (surfaces at 0.008 e/Å^3) in the: a) HS state and b) BS configuration. The blue areas correspond to α spin density, while the yellow ones to the β zones.

In the following we will do numeric experiments checking the interactions between boron atoms. In this view we will employ the so-called Broken Symmetry (BS) methods, performed in the DFT frame. The BS procedures are convenient procedures for estimate the exchange coupling parameters for phenomenological spin Hamiltonians accounting the magnetic properties of the transition metal complexes or stable radicals. Here we do not aim the account the magnetic properties of the boron doped diamond, although such samples can show, in principle, magnetic response. The exchange coupling parameters are in relation with the hopping integrals which are accounting the transferability of the electrons between different centers, being therefore am indirect

measure for the propensity for conducting properties. The BS procedure consists in a couple of calculations performed with unrestricted single-determinant methods, e.g. DFT. For a biradical system, one calculation, describes the conventionally labelled high spin (HS) configuration, with the spins in parallel alignment. Another calculation is devoted to the configuration having the broken symmetry (BS) quality, intentionally having the spin polarized with α density at one center and β on the other one. This is not a real state, since the singlet of a biradical made of 1 and 2 sites would imply a normalized ($\alpha_1\beta_2$-$\beta_1\alpha_2$) wavefunction composed from two Slater determinants. The BS configuration has a single determinant, $\alpha_1\beta_2$ or $\beta_1\alpha_2$. The quantity of interest is the gap between the HS and BS energies. More concretely, taking the negative of this gap, divided with the difference of expectation values of spin square operator (also found in the regular output of the calculation), taken in the same direction as the energy (say HS minus BS), yields the *J* exchange coupling parameter. A positive *J* value or a negative E_{HS}-E_{BS} difference represents a ferromagnetic coupling, namely a stable parallel alignment of the two spins. Conversely, the changed signs are signalling an antiferromagnetic situation, with a spin paired biradical.

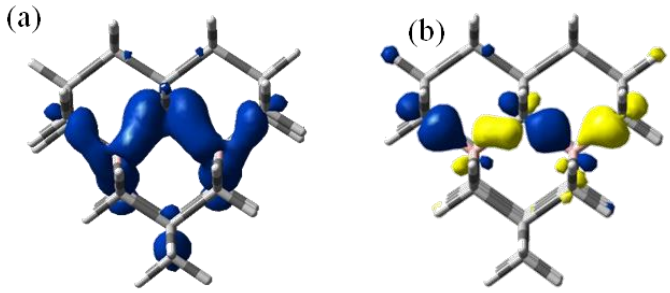

Fig. 19 The spin density maps for the $B_2C_{24}H_{32}$ molecule derived from pentamantane in the: a) HS state and b) BS configuration.

For a first glance, let us take a very simple model: the $C_4H_8B_2H_4$ molecule produced by the replacement of two CH_2 groups from the 1 and 4 positions in the cyclohexane ring, replaced with BH_2 units. The spin map of the HS state shows the tendency for delocalization of the unpaired electrons, comprising the whole skeleton. The BS map is not in the expected pattern, with α density grouped around one BH_2 group, while the β spins nearby the other. In turn, the spin polarization occurs as if the spin carriers are delocalized on the BC bonds. A similar pattern, is obtained in bigger carbon clusters, such as the skeleton of pentamantane $C_{26}H_{32}$ considered the smallest structural model of the diamond, obeying the T_d point group and mimicking the (111) face the diamond. In this case we replaced by boron atoms with 1-3 mutual placement in a C_6 ring. The free delocalization along the path of bonds connecting the B centers is noticed in Fig. 19. The smaller cases served for a clearer visualization of delocalization and spin polarization paths. Passing to more realistic environments for interacting boron centers simulating the doped boron we

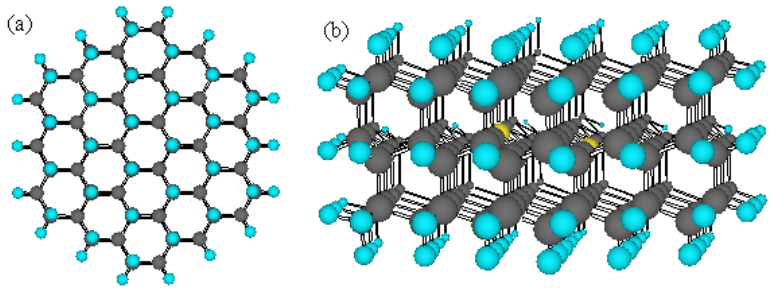

Fig. 20 Different orientations of the $C_{160}H_{108}B_2$ model molecule.

considered large molecules, $C_{160}H_{108}B_2$, consisting of three layers of fused hexagonal carbon rings in all-chair conformation. For clarity, the molecular skeleton of such a computation sample is shown in Fig. 20.

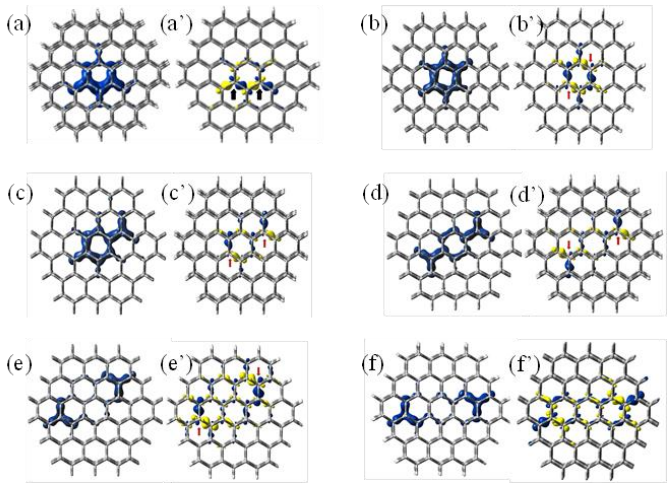

Fig. 21 Spin densities for a series of positional isomers of the $C_{160}H_{108}B_2$ determined at the BP86/6-31G level (contours of 0.008 e/Å^3). The boron atoms are placed in the middle plane of the triple decker molecule, in positions surrounded by the main concentration of HS spin density in each panel. The series (a)-(f) corresponds to HS results, while the (a')-(b') companions represent the BS companions. The separation between the boron sites in the selected cases is as follows: 2.548 Å (a), 2.989 Å (b), 4.414 Å (c), 5.910 Å (d), 7.380 Å (e), 7.808 Å (f)

The series of molecules and spin maps given in Fig. 21 are sampling the interaction between boron centers, viewed as generators of spin carriers, at different separation of their mutual placement. One may judge that the interaction is significant even in long range regime. In the HS maps, the delocalization along the carbon atoms path connecting the boron atoms is visible up to the separation of 4-5 Å represented in the (c) and (d) panels. At larger separations from the panels (e) and (f), of about 7-8 Å, the spins in the HS maps appear, visually, as isolated islands, but the BS drawings are yet showing a spin-polarization path traced between the sites (the alternation of α and β zones represented in blue and yellow coloring, respectively).

The features making the boron doped diamond suitable as electrode were investigated by computational experiments aiming to detect the local electron structure modifications induced in environment by a boron atom and the long range interaction between boron sites. We have found a rather strong communication between the B atoms, up to distances in the range of ten angstroms, a fact also in line with the conducting functionalities.

The above results were partially published in the following papers:

-„Platinum–carbon electrocatalytic composites via liposome-directed electrodeposition at conductive diamond" published in *International Journal of Hydrogen Energy* (2016) http://dx.doi.org/10.1016/j.ijhydene.2016.05.226.

-„Silica veils–conductive diamond powder composite as a new propitious substrate for platinum electrocatalysts" – *Journal of Solid State Electrochemistry*, Accepted for publication, DOI: 10.1007/s10008-016-3454-6.